MATERIALS SCIENCE

A pyrolyzed polyacrylonitrile/selenium disulfide composite cathode with remarkable lithium and sodium storage performances

Zhen Li, Jintao Zhang, Yan Lu, Xiong Wen (David) Lou*

As a special class of cathode materials for lithium-sulfur batteries, pyrolyzed polyacrylonitrile/sulfur (pPAN/S) can completely solve the polysulfide dissolution problem and deliver reliable performance. However, the applicable S contents of pPAN/S are usually lower than 50 weight % (wt %), and their capacity utilizations are not sufficient, both of which greatly limit their energy densities for commercial applications. We report a pyrolyzed polyacrylonitrile/selenium disulfide (pPAN/SeS_2) composite with dramatically enhanced active material content (63 wt %) and superior performances for both lithium and sodium storage. As a result, pPAN/SeS_2 delivers high capacity of >1100 mAh g^{-1} at 0.2 A g^{-1} for Li storage with extremely stable cycle life over 2000 cycles at 4.0 A g^{-1}. Moreover, when applied in a room temperature Na-SeS_2 battery, pPAN/SeS_2 achieves superior capacity of >900 mAh g^{-1} at 0.1 A g^{-1} and delivers prolonged cycle life over 400 cycles at 1.0 A g^{-1}.

INTRODUCTION

There has been increasing demand for high–energy density and long–cycle life rechargeable batteries to address pressing needs for many emerging applications, such as electric vehicles, portable electronics, and grid energy storage (*1*). Because of the high theoretical capacity and natural abundance of sulfur, lithium-sulfur (Li-S) batteries present nearly threefold higher energy density and are more cost-effective than the state-of-the-art commercial Li-ion batteries (*2*). The major problems that hinder the practical applications of Li-S batteries are the insufficient capacity utilization, low energy efficiency, limited cycle life, and fast self-discharge, all of which are mainly caused by the insulating nature of S and the dissolution of long-chain lithium polysulfides (Li_2S_x, $x \geq 4$, noted as LiPSs) into liquid electrolyte (*3*). As a resolution, conductive hosts with porous/hollow structures are designed and applied to increase the utilization ratio of S and reduce the dissolution of LiPSs (*4*–*6*). Although the electrochemical performance of Li-S batteries can be obviously improved by the rationally designed electrode structures, it must not be ignored that dissolution in organic electrolyte is the intrinsic nature of long-chain LiPSs; thus, the generation and migration of LiPSs could not be ultimately overcome as long as the normal ring-structured S_8 molecule–based cathodes and the ether-based electrolytes are used in the batteries (*7*, *8*).

Fortunately, it is found that, when S molecules are chemically bonded onto polymer backbones or confined within microporous carbons, the LiPS dissolution issue can be entirely eliminated (*9*–*13*). On the basis of this special class of cathode materials, the cycling stability of Li-S batteries has been greatly improved (*14*, *15*). Moreover, these cathodes are chemically matched with the industrially used $LiPF_6$-carbonate–based electrolytes, so there is a great potential for them to couple with many mature anodes for developing Li-ion batteries with high energy density, low cost, good safety, and reliability (*16*–*18*). Compared to microporous carbon materials, which usually require multistep preparation, polyacrylonitrile (PAN) has been thought as a much better precursor for composing with sulfur species. Because of the easiness to dehydrogenate and cyclize into conjugated backbones, the pyrolyzed PAN/sulfur (pPAN/S) composite can be prepared through a facile one-step reaction of PAN with commercial S powder at elevated temperature (*19*, *20*). Previous studies have successfully revealed the electrochemical reaction mechanisms of pPAN/S for lithium storage (*15*, *21*–*24*) and introduced conductive additives into the pPAN/S composites to further enhance their capacity utilizations (*25*–*28*). However, the S content of pPAN/S is usually less than 50 weight % (wt %), which leads to an obvious lower energy density compared to the normal S_8-based composite cathodes with the loading of ≥60 wt % of S (*19*). Because the concentration of functional groups in pPAN backbones is limited, it seems not possible to bond more S in the pPAN/S composite.

Besides the low S content issue, another challenge is the relatively low capacity utilization of the pPAN/S cathode because of the insulating nature of S and the polymer backbones. Therefore, to make the pPAN-supported cathodes more practical, it is of great importance to explore new-concept cathode materials with higher content of active materials and better reaction kinetics. Similar with S, selenium (Se) can be applied as the cathode for Li and Na storage via alloying reactions, but with much enhanced kinetics because of its orders of magnitude higher conductivity (*29*, *30*). Moreover, Li/Na-Se batteries could facilely achieve prolonged cycle life without shuttle effect in carbonate electrolyte (*31*–*33*). Some recently reported Se-based composites have shown excellent electrochemical performances accompanied with high volumetric energy density (*34*–*37*). However, the theoretical gravimetric energy density of Se is not high, and the material cost of Se is much higher than S, both of which limit the application potential of pure Se-based cathode materials. Therefore, it might be a more rational approach to use Se_xS_y solid solution as the active material for energy storage (*38*–*41*).

Here, we report a novel pyrolyzed PAN/selenium disulfide (pPAN/SeS_2) composite as a cathode material for lithium and sodium storage. Benefiting from the novel multichannel structure and the relatively higher density of SeS_2, the active material content of pPAN/SeS_2 reaches 63 wt %. Because of the better conductivity of SeS_2 than S, the electrochemical reaction kinetics of pPAN/SeS_2 are remarkably boosted. As a result, the Li-SeS_2 battery based on the pPAN/SeS_2 cathode delivers high capacity, excellent C-rate property, and extremely stable cycle life over 2000 cycles. When applied in a room temperature Na-SeS_2 (RT Na-SeS_2) battery, the pPAN/SeS_2 cathode shows superior capacity

School of Chemical and Biomedical Engineering, Nanyang Technological University, 62 Nanyang Drive, Singapore 637459, Singapore.
*Corresponding author. Email: xwlou@ntu.edu.sg

of >900 mAh g^{-1} at a current density of 0.1 A g^{-1} and delivers prolonged cycle life over 400 cycles.

RESULTS

Materials synthesis and characterization

The pPAN/SeS_2 composite cathode is prepared by a facile strategy, which involves a simple heating treatment of the mixture of the PAN/PS fibers and commercial SeS_2 powder (fig. S1). The precursor of PAN/PS fibers was prepared by an electrospinning method reported by our group elsewhere (*42*). During the heating process, PAN reacts with gasified SeS_2, and the PS component would decompose and generate a series of paralleled channels inside the composite fibers. The as-prepared pPAN/SeS_2 product well maintains the one-dimensional (1D) morphology with large aspect ratio, and the diameters of the fibers are in the range of 1.4 to 2 μm (Fig. 1, A and B). A cross-section image directly shows the unique multichannel structure of pPAN/SeS_2 (Fig. 1C). The highly paralleled channels are uniformly running through every pPAN/SeS_2 fiber (Fig. 1, D and E). Compared to solid particles, the hollow channels inside pPAN/SeS_2 will be beneficial for better infiltration of electrolyte and then achieve superior ion conductivity accordingly. No additional SeS_2 particles can be observed on the surface or inside the channels of the pPAN framework, and the pPAN/SeS_2 composite shows an amorphous phase without any crystal lattice image in its structure (Fig. 1F). These observations indicate that SeS_2 is well composed with pPAN after the heat treatment. Elemental mappings further confirm that Se and S are uniformly distributed within the pPAN framework (Fig. 1G and fig. S2). The compact density of the pPAN/SeS_2 composite is measured to be 0.78 g cm^{-3}. To verify the structural advantage of the multichannel design for increasing the SeS_2 content, a control sample of powder-pPAN/SeS_2 is prepared (Fig. 1H). Thermogravimetric analysis (TGA) results show that these multichannel pPAN/SeS_2 fibers can be loaded with 63 wt % of SeS_2 within the framework, which is obviously higher than that of the powder-pPAN/SeS_2 composite (49 wt %) (Fig. 1I). It is proposed that, compared to solid particles, the multichannel framework can provide more surface area of PAN to directly contact and fully react with SeS_2 (fig. S3). In addition, there might be some small pores generated by PS (*42*), which can firmly trap part of SeS_2 even after an additional treatment at 300°C for 4 hours in flowing N_2 atmosphere. Another two samples of pPAN/S and pPAN/Se are prepared by the same method as control groups. The morphologies of these two control samples are the same with pPAN/SeS_2 (fig. S4), and the mass ratios of S and Se in pPAN/S and pPAN/Se are 52 and 65 wt %, respectively (fig. S5). The differences on active material contents are mainly caused by the different molar mass of S, SeS_2, and Se. When the same molar quantity of S, SeS_2, and Se molecules is bonded onto the polymer backbones, the heavier element might gain higher mass loading content in the final composite. It is noteworthy that the SeS_2 content of multichannel pPAN/SeS_2 is higher than previously reported similar composites (*19*, *43*), which further confirms the structural and componential advantages of our design for increasing the active material ratio (fig. S6).

After the heat treatment, the derived pPAN/SeS_2 shows an amorphous phase without any signal of pristine SeS_2 (Fig. 2A), which is consistent with the high-resolution TEM observation. Fourier transform infrared (FTIR) spectra show the changes of organic functional groups from PAN to pPAN/SeS_2 (Fig. 2, B and C). After reacting with SeS_2 at an elevated temperature (380°C), the –CH, $–CH_2$, and –CN groups on PAN vanish, while some new bonds/groups of C=C (1485 cm^{-1}), –CH (1356 cm^{-1}), and cyclic structure (1436 and 802 cm^{-1}) emerge,

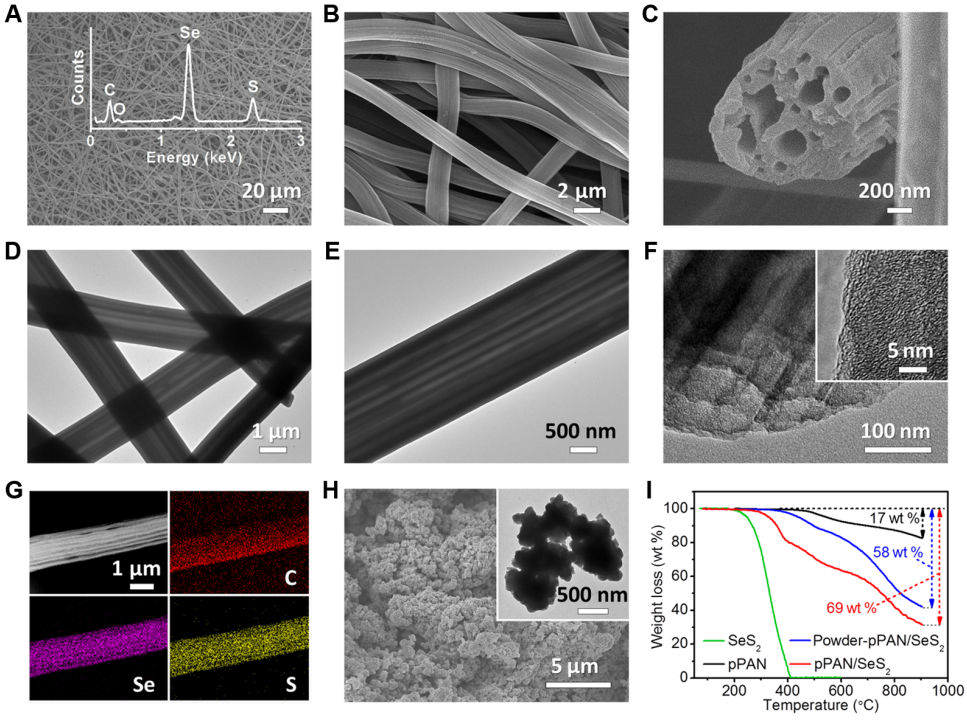

Fig. 1. Morphology and structure characterizations of pPAN/SeS_2. (**A** to **C**) Scanning electron microscopy (SEM) images, (**D** to **F**) transmission electron microscopy (TEM) images, (**G**) dark-field TEM image, and corresponding elemental mappings of pPAN/SeS_2. (**H**) SEM and TEM images of powder-pPAN/SeS_2. (**I**) TGA curves of SeS_2, pPAN, pPAN/SeS_2, and powder-pPAN/SeS_2. Inset of (A) shows the energy-dispersive x-ray (EDX) plot of pPAN/SeS_2.

indicating the formation of heterocyclic compounds during the dehydrogenation reaction with SeS_2 (*23*, *44*). During this dehydrogenation process, Se-S chains are chemically bonded to the polymer backbones simultaneously. Raman spectra are collected to further determine the structure of SeS_2 in the composite (Fig. 2D). After composing with PAN, three characteristic peaks of bare SeS_2 are replaced with one peak in pPAN/SeS_2, and its position shifts to 228 cm^{-1}. This suggests that the ring-structured SeS_2 molecules have been transformed to chain-like Se_xS_y molecules, which is similar with the S chains covalently bonded onto the polymer backbones (*23*). XPS spectrum of C 1s reveals the chemical bonds between Se/S and C (Fig. 2E), and the spectrum of S 2p and Se 3p shows the strong interaction between Se and S (Fig. 2F), reflecting that Se and S are bonded simultaneously in the chain-like Se-S molecules (*43*, *45*).

The electrochemical performances

To show the differences on electrochemical behaviors of pPAN/SeS_2, pPAN/S, and pPAN/Se, coin cells of three samples are prepared in the same way using Li metal as the anode. By comparing the electrochemical impedance spectroscopy (EIS) plots of three samples, it can be seen that the conductivity of the active material has direct effects on the interfacial resistance of the derived electrode films (fig. S7). Compared to pPAN/S, pPAN/SeS_2 shows obviously reduced interfacial resistance of the electrode. Figure 3A compares the typical galvanostatic discharge-charge voltage profiles at 0.5 A g^{-1}. The pPAN/SeS_2 cathode delivers a specific capacity of 1031 mAh g^{-1} and an average discharge voltage plateau of 1.76 V at 50% depth of discharge, both of which are higher than that of the pPAN/S and pPAN/Se cathodes. Although the theoretical capacity of S (1672 mAh g^{-1}) is higher than that of SeS_2 (1123 mAh g^{-1}), the insulating nature of S greatly affects the reaction kinetics of the pPAN/S cathode, which increases the polarization during the redox reaction and limits the capacity utilization. Because of the good conductivity of Se, the pPAN/Se electrode delivers a capacity of 629 mAh g^{-1}, corresponding to an excellent utilization ratio (93%) to its theoretical capacity (678 mAh g^{-1}). However, the pPAN/Se cathode provides the lowest energy density among all three cathodes because of its much lower capacity (fig. S8). The comparison of cyclic voltammetry (CV) curves at 0.2 mV s^{-1} shows differences on the cathodic/anodic peak positions and areas, which indicates that pPAN/SeS_2 has a better balance on reaction kinetics and capacity releasing compared to pPAN/S and pPAN/Se (Fig. 3B).

The reaction kinetics of pPAN/SeS_2, pPAN/S, and pPAN/Se is further analyzed based on CV measurements at various scan rates (Fig. 3C and fig. S9). The results show that, for all groups, both the peak current and the potential polarization increase with the scan rate. Because the current changes with respect to the sweep rate can be expressed as $i = a \cdot v^b$ (where i is the peak current, v is the scan rate, and a and b are the adjustable constants), it is possible to mathematically analyze the reaction kinetics by comparing the b values of various groups (*35*, *46*). The b values of pPAN/SeS_2 in both cathodic (b_c) and anodic (b_a) processes are similar with pPAN/Se and much higher than that of pPAN/S, demonstrating that the introduction of Se can effectively improve reaction kinetics of the electrode material (Fig. 3D). The Li^+-ion diffusion coefficients of three groups are calculated via the galvanostatic intermittent titration technique (GITT) during discharge/charge processes (Fig. 3, E and F). The results show that the Li^+-ion diffusion coefficients of pPAN/SeS_2 and pPAN/Se are nearly one order of magnitude higher than that of pPAN/S, which reveals that the Li^+-ion diffusion in the redox reactions is greatly improved benefiting from the presence of Se. On the basis of the above results, it can be concluded that, when a certain content of Se is introduced into the pPAN/S composite, both the electronic conductivity and the ionic diffusion efficiency in the cathode material can be effectively enhanced.

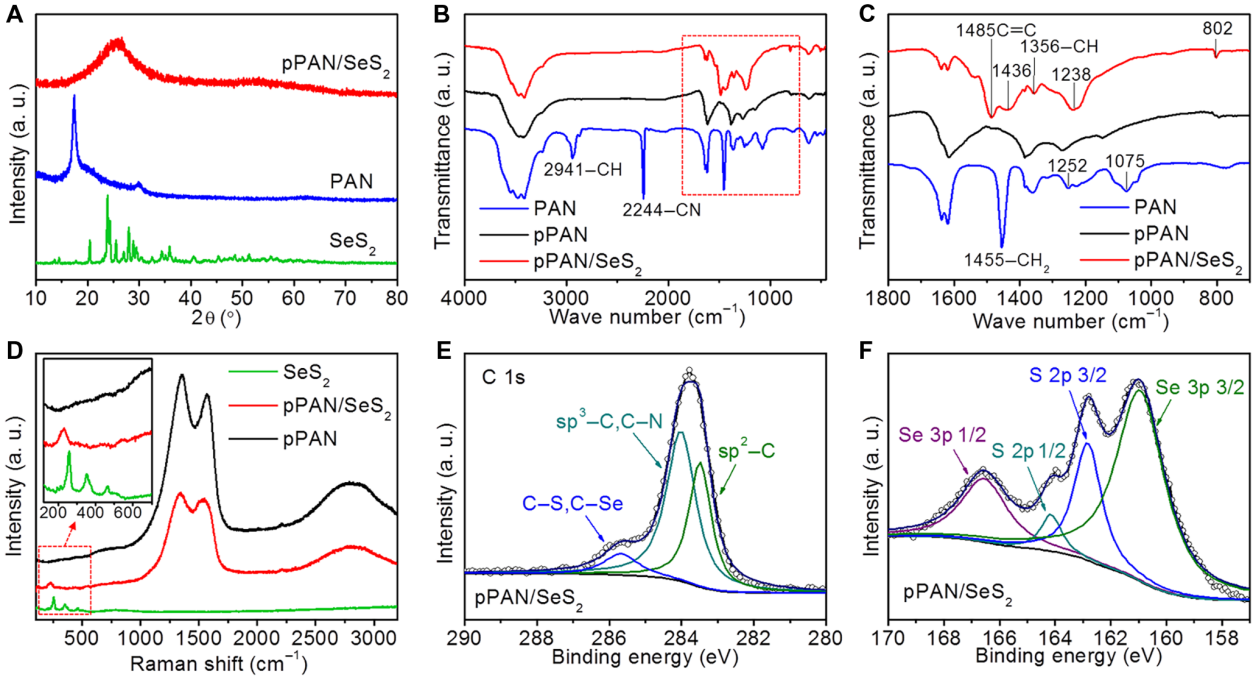

Fig. 2. Characterizations of pPAN/SeS_2 and the control samples. (**A**) X-ray diffraction (XRD) patterns, (**B** and **C**) FTIR, and (**D**) Raman spectra of pPAN/SeS_2 and the control samples (SeS_2, PAN, and pPAN). X-ray photoelectron spectroscopy (XPS) spectra of (**E**) C 1s and (**F**) S 2p/Se 3p for pPAN/SeS_2. a.u., arbitrary units.

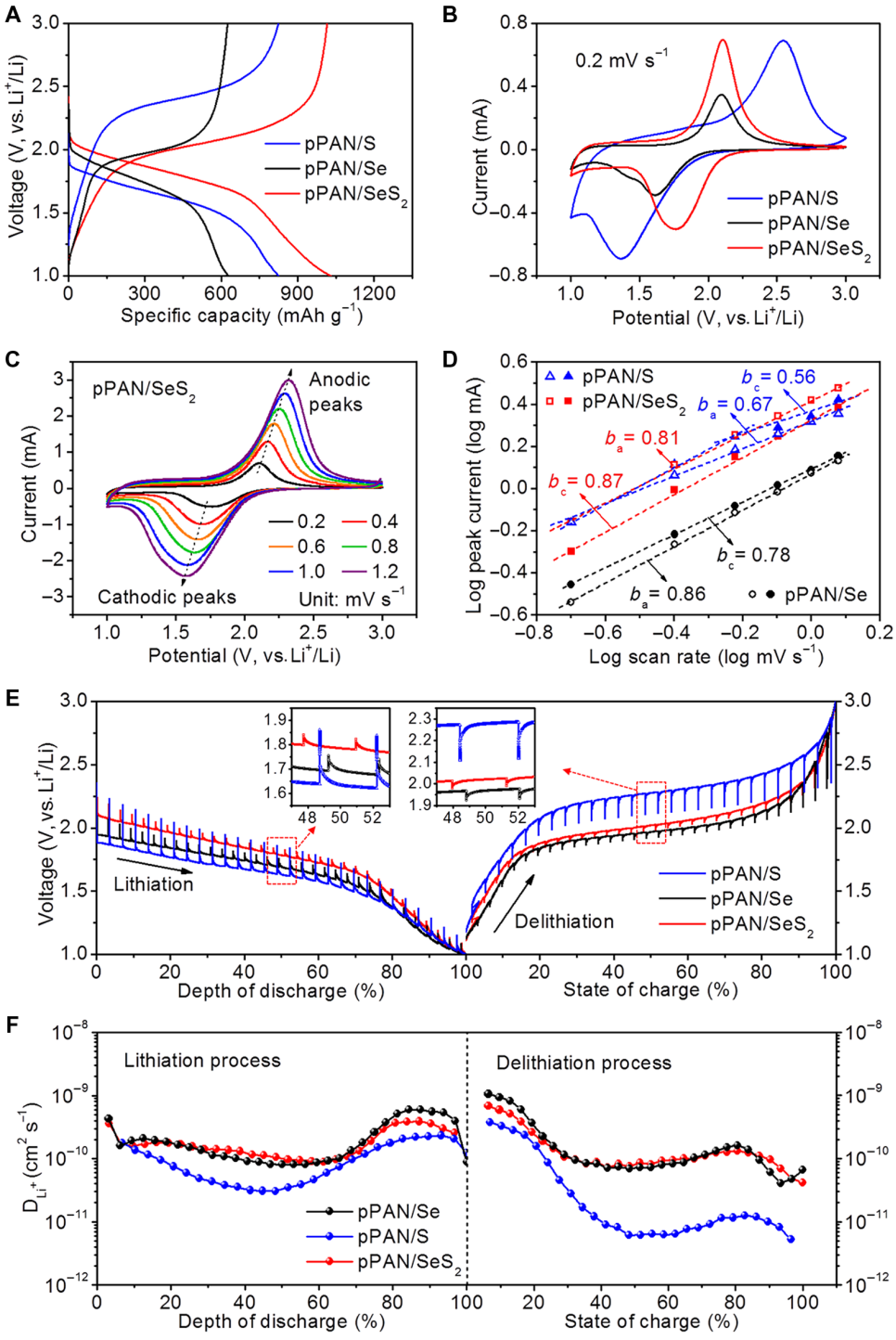

Fig. 3. Electrochemical evaluation of pPAN/S, pPAN/SeS_2, and pPAN/Se. Comparisons of (**A**) typical voltage profiles at 0.5 A g^{-1}, and (**B**) CV curves at 0.2 mV s^{-1} of pPAN/SeS_2, pPAN/S, and pPAN/Se. (**C**) CV curves of pPAN/SeS_2 from 0.2 to 1.2 mV s^{-1}. (**D**) Comparison of *b* values in the cathodic (b_c) and anodic (b_a) scans from 0.2 to 1.2 mV s^{-1} of different groups. *b*-value determination based on logarithmic peak currents versus scan rate. Voltage profiles (**E**) and the Li-ion diffusion coefficients (**F**) of pPAN/SeS_2, pPAN/S, and pPAN/Se obtained via the GITT technique during discharge/charge processes.

The pPAN/SeS_2 cathode exhibits superior cycling stability similar to as previously reported pPAN-supported S-based cathodes (*9*, *15*, *21*). When cycled at 0.5 A g^{-1}, the pPAN/SeS_2 cathode delivers a capacity of 1451 mAh g^{-1} in the initial discharge, and then the capacities stabilize at around 1020 mAh g^{-1} in subsequent cycles with Coulombic efficiency of nearly 100% (Fig. 4A). The lower discharge plateaus and the irreversible capacity in the first discharge are mainly caused by the reduction of electrolyte solvents on the fresh surface of electrode materials for the

formation of solid electrolyte interface (*43*, *47*, *48*). Although the released capacity is very stable even in the first 10 cycles, it is observed that the discharge voltage plateaus gradually increase with the cycle times, indicating that there is an electrochemical activation process in the cathode (Fig. 4B). Similar phenomena are also observed in the pPAN-supported Se or S-based cathodes in previous studies (*44*, *45*). After that, the discharge plateaus are stabilized, and the typical voltage profiles of the 50th and 100th cycles are well matched with each other, demonstrating very good stability of the pPAN/SeS_2 cathode. The comparison of high-rate capabilities further supports the superiority of pPAN/SeS_2 over pPAN/S and pPAN/Se (Fig. 4, C and D). Upon cycling at current densities of 0.2, 0.5, 1, 2, 3, 4, and 5 A g^{-1}, the pPAN/SeS_2 cathode delivers reversible capacities of 1117, 1053, 992, 904, 839, 774, and 709 mAh g^{-1}, respectively (Fig. 4D). When the rate is reduced back to 0.2 A g^{-1}, the capacity of pPAN/SeS_2 regains 1115 mAh g^{-1}, indicating excellent electrochemical stability of the cathode material. In contrast, the pPAN/S cathode delivers lower discharge capacities at various current densities (fig. S10). When the current density is increased to 5 A g^{-1}, the pPAN/S cathode only delivers a capacity of 85 mAh g^{-1}, corresponding to a poor retention ratio of 9% versus the early capacity of 971 mAh g^{-1} at 0.2 A g^{-1}. The relatively poor performance of pPAN/S compared to some previously reported pPAN/S composites might be caused by the higher S content (52 wt %), which may easily lead to a higher polarization and decrease the capacity utilization.

It is noted that pPAN/Se achieves the best capacity retention ratios in the C-rate tests among three groups (fig. S11), demonstrating that Se is a good constituent material for enhancing the reaction kinetics of the cathode materials. However, limited by the low theoretical capacity of Se, the specific capacities of pPAN/Se are much lower than those of pPAN/SeS_2, which affect the gravimetric/power energy densities of the Li-Se battery (Fig. 4, E and F). Therefore, the pPAN/SeS_2 composite cathode might be a more rational choice for Li storage because it inherits advantages of both pPAN/Se and pPAN/S. Moreover, the pPAN/SeS_2 cathode promises extremely stable cycle life (Fig. 4G). After an activation process of three cycles at 0.2 A g^{-1}, the pPAN/SeS_2 cathode is cycled at a higher current density for 2000 cycles. The pPAN/SeS_2 cathode delivers a capacity of 871 mAh g^{-1} when first discharged at 4 A g^{-1}, and it keeps a discharge capacity of 633 mAh g^{-1} at the end of the test, corresponding to a very low capacity decay rate of 0.014% per cycle. To reveal the commercial application potential of pPAN/SeS_2, a thick electrode with pPAN/SeS_2 loading of 7.9 mg cm^{-2} is further evaluated (Fig. 4H). Over 50 cycles at 0.2 A g^{-1}, the specific capacity of SeS_2 is remarkably stable at >900 mAh g^{-1}, corresponding to a high areal capacity of >4.5 mA cm^{-2}.

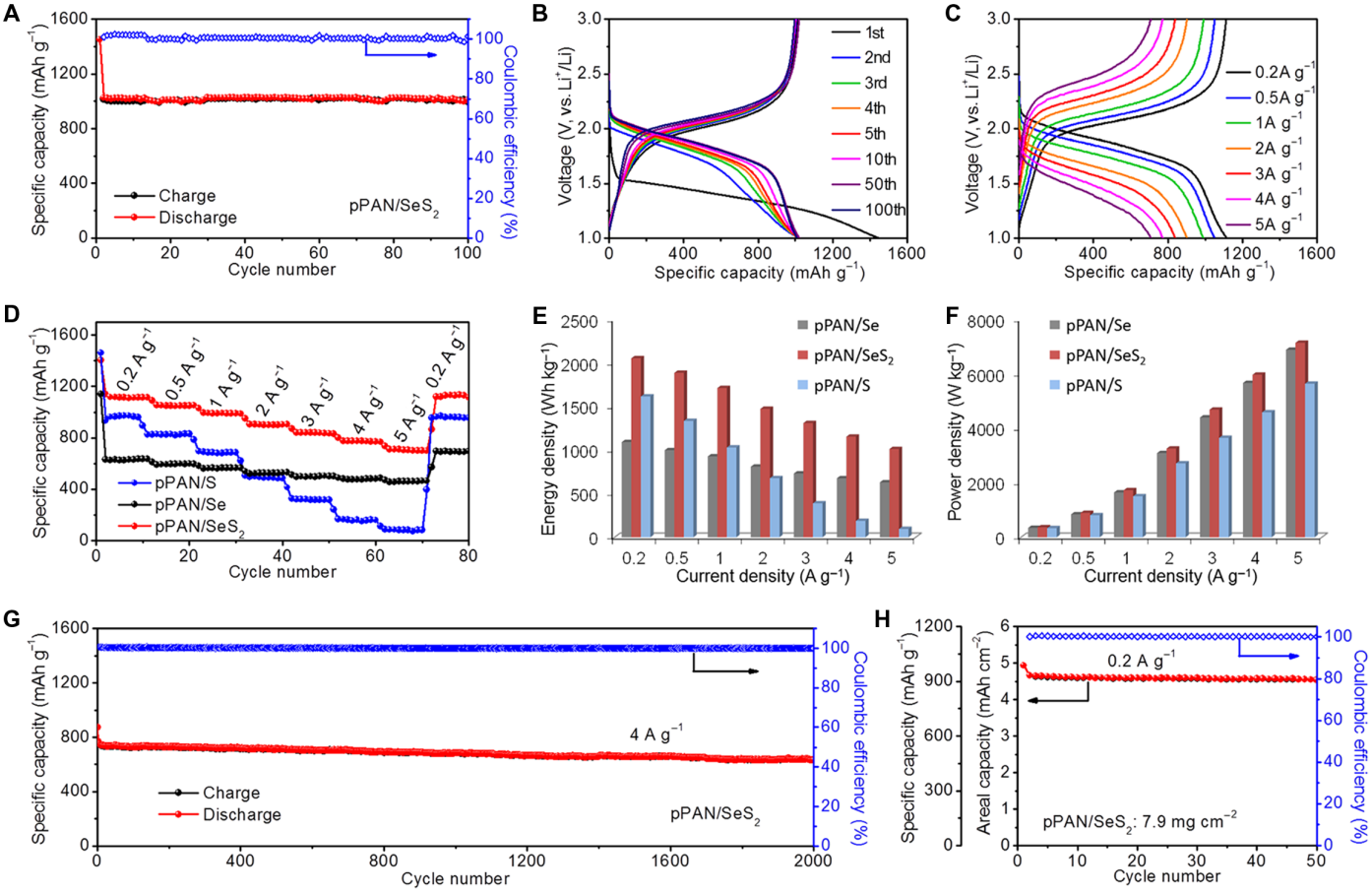

Fig. 4. Electrochemical performance of Li-SeS_2 battery. (**A**) Cycle property at 0.5 A g^{-1}. (**B**) Voltage profiles during cycle test. (**C**) Voltage profiles at various current densities from 0.2 to 5 A g^{-1} of pPAN/SeS_2. Comparisons of (**D**) rate performance from 0.2 to 5 A g^{-1}, (**E**) energy density, and (**F**) power density of pPAN/Se, pPAN/SeS_2, and pPAN/S. (**G**) Prolonged cycle life at 4 A g^{-1}, and (**H**) cycling property at 0.2 A g^{-1} with high areal mass loading of pPAN/SeS_2 for Li storage.

Recently, the room temperature sodium-sulfur (RT Na-S) battery has attracted much attention in view of its tremendous potential for reducing the cost and improving the safety of traditional high-temperature Na-S battery systems (*47*, *49*–*52*). However, because of the poor electronic and ionic conductivity of S and Na_2S, the reaction kinetics of RT Na-S batteries could not be easily improved. It is still a big challenge to further enhance the capacity utilization of RT Na-S batteries. Here, because pPAN/SeS_2 shows much higher reactivity than pPAN/S for Li storage, it is thus anticipated that the pPAN/SeS_2 composite could give better Na-storage performance than previous S-based cathodes. When evaluated as a cathode material for Na storage, the CV curves and voltage profiles of pPAN/SeS_2 show very similar electrochemical features with the Li-SeS_2 battery (fig. S12). After an initial activation, the RT Na-SeS_2 battery shows two discharging plateaus in voltage ranges of 2.8 to 1.2 and 1.2 to 0.8 V. The lower-voltage plateaus may be caused by a stepped reduction reaction between SeS_2 and Na (*35*, *37*, *47*). Figure 5A shows the comparison of cycling properties between pPAN/SeS_2 and pPAN/S for Na storage. By using pPAN/SeS_2 as the cathode, the RT Na-SeS_2 battery delivers a high capacity of 1530 mAh g^{-1} at 0.1 A g^{-1} in the first discharge, and then its capacity stabilizes at 944 mAh g^{-1} at the second cycle. After 50 cycles, pPAN/SeS_2 still maintains a high capacity of 835 mAh g^{-1}, which is much higher than the specific capacity of S in high-temperature Na-S batteries (*53*). On the contrary, although pPAN/S gains a high initial capacity of 1264 mAh g^{-1}, the capacity decreases rapidly to 331 mAh g^{-1} after 50 cycles. Moreover, the average discharge plateau of pPAN/SeS_2 is obviously higher than that of pPAN/S (Fig. 5B), demonstrating that the pPAN/SeS_2 cathode is beneficial to achieve a higher energy density than pPAN/S for Na storage. pPAN/SeS_2 exhibits excellent Na storage capabilities at various current densities. The RT Na-SeS_2 battery maintains a capacity of 938 mAh g^{-1} at 0.1 A g^{-1} and then delivers 869, 802, 736, 634, 583, 471, and 302 mAh g^{-1} when the current density is successively increased from 0.2 to 0.5, 1, 2, 3, 4, and 5 A g^{-1}, respectively (Fig. 5, C and D). For the RT Na-S battery, the pPAN/S cathode shows a reversible capacity of 813 mAh g^{-1} when first cycled at 0.1 A g^{-1}. Subsequent cycling at different current densities from 0.2 to 4 A g^{-1} reveals that the rate capabilities of pPAN/S are inferior to those of pPAN/SeS_2. When the current density is abruptly turned back to 0.1 A g^{-1} from 4 A g^{-1}, the pPAN/SeS_2 cathode recovers all of the original capacity, indicating the superior robustness and reversibility of the electrode. Prolonged cycle life of the RT Na-SeS_2 battery is evaluated under 1 A g^{-1} (Fig. 5E). The pPAN/SeS_2 cathode delivers a high initial capacity of 1043 mAh g^{-1} and maintains a reversible capacity of 800 mAh g^{-1} after 400 cycles, indicating an extremely stable cycle life. Compared

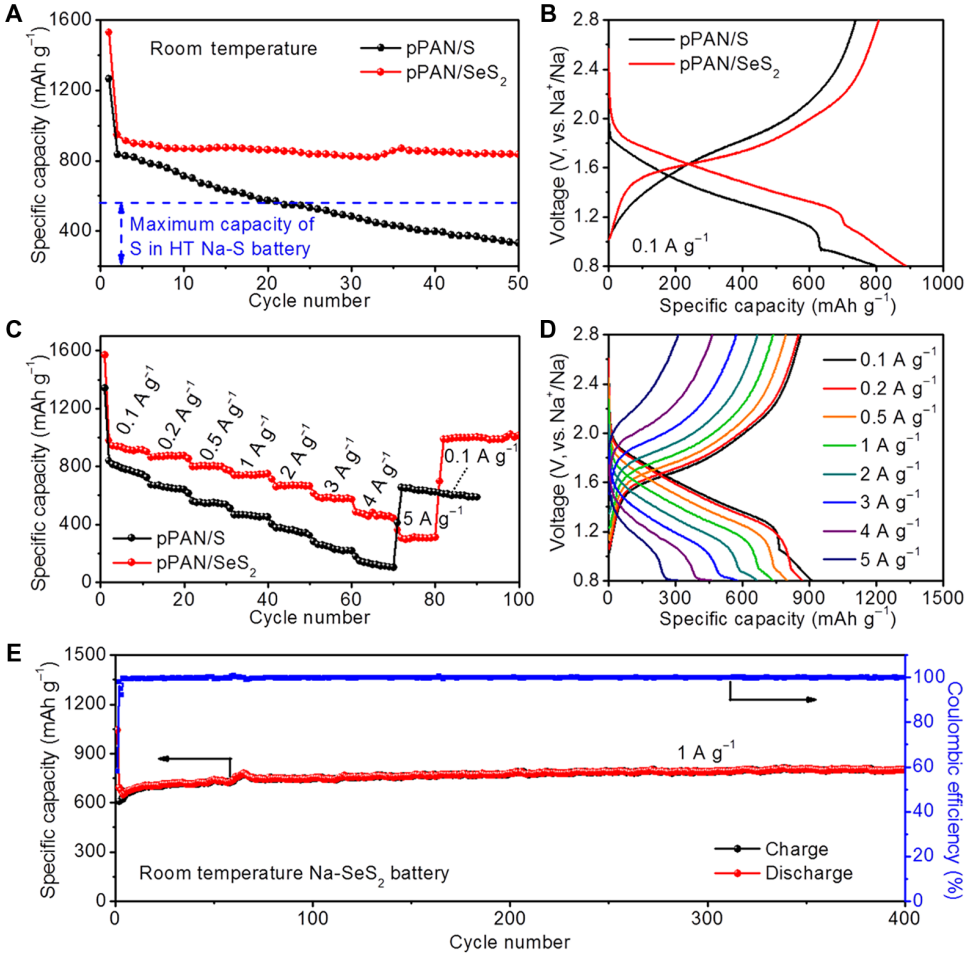

Fig. 5. Electrochemical performance of RT Na-SeS_2 battery. Comparisons of (**A**) cycle stabilities at 0.1 A g^{-1}, (**B**) typical voltage profiles, (**C**) and rate performances between pPAN/S and pPAN/SeS_2. (**D**) Voltage profiles at various current densities from 0.1 to 5 A g^{-1}. (**E**) Prolonged cycle life of pPAN/SeS_2 for Na storage.

to previously reported RT Na-S batteries, our RT Na-SeS_2 battery shows significant advantages on both active materials content and overall capacities of the composite cathodes (fig. S13).

DISCUSSION

Many spectroscopic characterizations have consistently identified that sulfur molecules in the sulfurized PAN exist in the form of short $-S_x-$ chains covalently bonded to the cyclized and dehydrogenated PAN backbones through C–S bonds (*21*, *23*, *24*). It can be speculated that, in the pPAN/SeS_2 composite, there might be short $-Se_xS_y-$ chains covalently bonded to PAN backbones through C–S and/or C–Se bonds. Because the mole fraction of Se is as high as one-third, it is highly possible that Se may be present in every active short chain. Because of the excellent reaction kinetics of Se, the presence of Se in the short $-Se_xS_y-$ chains will greatly enhance the reactivity of the electrode material. Thus, the diffusivity and voltage profile of pPAN/SeS_2 are akin to the pure Se-based pPAN/Se cathode rather than pPAN/S.

To reveal the structural and chemical stability of pPAN/SeS_2, the Li-SeS_2 coin cells have been disassembled for further characterization. After cycling for 100 cycles, the pPAN/SeS_2 electrode film maintains similar morphology with the fresh electrode film (Fig. 6, A and B), and the cathode material is still strongly adhered on the current collector without any visible cracking (Fig. 6C), proving that the electrode film is robust enough to endure the electrochemical tests. The separator dissembled from the cycled coin cell well maintains its original morphology, and the porous structure can be observed as before (Fig. 6D), while the surface of the Li metal anode becomes rough because of many cycles of Li plating/stripping (Fig. 6E). Besides the morphological observations, it is more remarkable that no Se or S can be detected on the surfaces of both the separator and the Li metal anode (insets of Fig. 6, D and E), which implies that the dissolution of polysulfides/polyselenides is completely avoided in the pPAN/SeS_2-based battery system. Meanwhile, the EDX results show that the chemical compositions of the pPAN/SeS_2 electrode films are almost the same with each other during the cycling process (Fig. 6F), thus directly confirming the good chemical stability of pPAN/SeS_2.

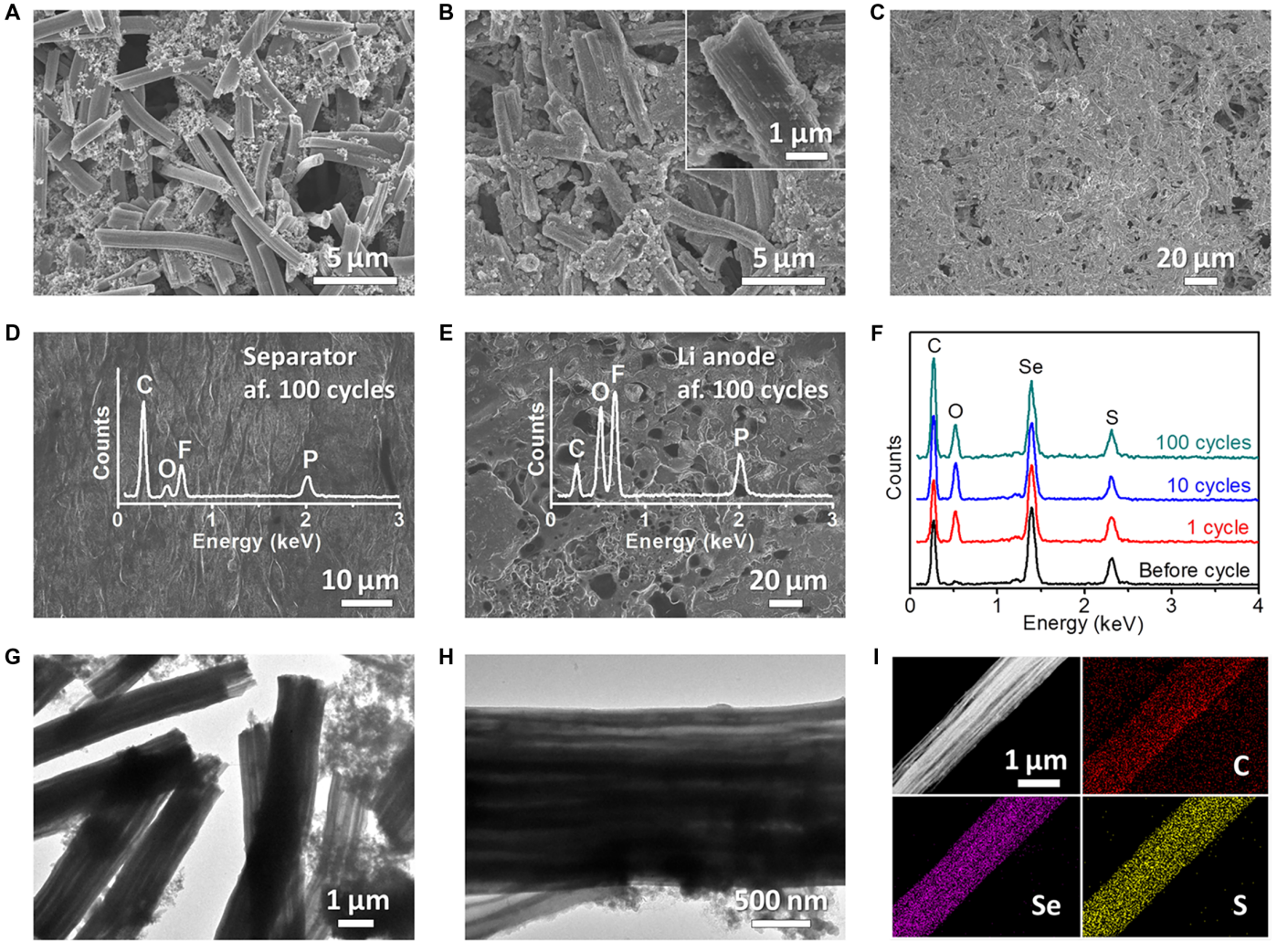

Fig. 6. Characterizations of pPAN/SeS_2 after cycling tests. SEM images of (**A**) fresh and (**B** and **C**) 100 times cycled pPAN/SeS_2 electrode films. SEM images of (**D**) separator and (**E**) Li anode disassembled from the pPAN/SeS_2 cells after 100 cycles. Insets of (D), (E), and (**F**) are EDX plots of separator, Li anode, and cathode films, respectively. (**G** and **H**) TEM images and (**I**) elemental mappings of pPAN/SeS_2 after 100 cycles for Li storage.

In addition, the 1D morphology of the pPAN/SeS_2 fibers is well preserved (Fig. 6G), and the internal channels can still be observed (Fig. 6H), revealing the robust and reliable feature of the multichannel structure. The elemental mappings show the uniform distributions of Se and S in the pPAN polymer backbones (Fig. 6I), further confirming the good chemical stability of pPAN/SeS_2.

In summary, pPAN/SeS_2 fibers with the multichannel structure have been designed and prepared by a facile method. This nanocomposite successfully inherits advantages of both pPAN/S and pPAN/Se and avoids their drawbacks. The active material content of the pPAN-supported composites has been elevated to a new level. When applied as cathode materials for Li and Na storage, pPAN/SeS_2 fibers show excellent reaction kinetics, high capacity utilizations, robust material structure, and remarkable electrochemical stability. Besides, it should be pointed out that although the molar ratio of Se/S (1:2) has given a much better balance on reaction kinetics and capacity than bare S and Se, there might be more space for optimizing the S-to-Se ratio for gaining specific cost/performance balance for different applications. It is thus believed that the composite cathode material reported here might have a great potential for building better batteries beyond traditional lithium ion batteries.

MATERIALS AND METHODS

Synthesis

One gram of PAN and 0.8 g of polystyrene (PS) were dissolved in 10 ml of *N*,*N*-dimethylformamide with vigorous stirring at 60°C overnight. Then, the PAN/PS composite nanofibers were prepared by the electrospinning method. A high voltage of 17 kV was applied with a flow rate of 1 ml h^{-1}, and the distance between the syringe and the collector was 15 cm. Then, the derived PAN/PS fibers and the commercial SeS_2 powder (1:4, w/w) were sealed in a glass vessel and heated at 380°C for 8 hours in N_2 atmosphere. To remove extra SeS_2, the sample was put in a porcelain boat and heated at 300°C for 4 hours in flowing N_2 atmosphere. After the temperature is decreased below 50°C, pPAN/SeS_2 was gained. Similarly, both pPAN/S and pPAN/Se were prepared by the same method, only using S or Se instead of SeS_2 for the reaction, respectively. A control sample of powder-pPAN/SeS_2 was prepared by heating the mixture of commercial PAN powder and SeS_2 in a sealed glass vessel at 380°C for 8 hours in N_2 atmosphere, and then the product was put in a porcelain boat and heated at 300°C for 4 hours in a flowing N_2 atmosphere. The pure pPAN was prepared by heating PAN/PS at 380°C for 8 hours in an N_2 atmosphere.

Materials characterization

SEM (JEOL-6700F) and TEM (JEOL, JEM-2010) were used to characterize the morphologies and structures of the samples. Elemental mappings were recorded by EDX spectroscopy attached to TEM (JEOL, JEM-2100F). Compositions of electrode films, separator, and Li anode were measured by EDX spectroscopy attached to the SEM instrument. The XRD patterns were measured by a Bruker D2 phaser (Cu Kα radiation λ = 1.5406 Å). Raman spectra were examined by a Renishaw System 1000 micro-Raman spectroscope with 514-nm excitation source. FTIR spectra were collected with Bruker MPA NearIR. Active material contents were determined by TGA (Shimadzu DRG-60) in N_2 flow. XPS was carried out on a Thermo Fisher Scientific ESCALAB 250Xi. The nitrogen sorption isotherms were collected by a Quantachrome Autosorb AS-6B system at liquid-nitrogen temperature. To determine the compact density of the material, pPAN/SeS_2 was pressed into pellets at 10 MPa, and then the compact density was calculated based on the mass and volume of the pellets.

Electrochemical measurements

The electrode film of pPAN/SeS_2 was prepared by mixing pPAN/SeS_2, Super-P, carboxymethylcellulose, and styrene butadiene rubber with a mass ratio of 8:1:0.5:0.5 in deionized water, and then the slurry was casted on the Al foil and dried at 70°C overnight. The areal mass loading of pPAN/SeS_2 was around 2.0 mg cm^{-2}. High–mass loading electrode films were prepared by coating the same slurry on carbon papers. CR2032 coin cells were assembled in an Ar-filled glove box. For Li-SeS_2 batteries, Li metal was applied as the anode, and Celgard 2400 membrane was applied as the separator. The electrolyte was 1.0 M $LiPF_6$ in ethylene carbonate (EC) and dimethyl carbonate (DMC) (1:1, v/v). The SeS_2/electrolyte ratio is around 1 mg/50 μl. For RT Na-SeS_2 batteries, Na metal was applied as the anode and Whatman glass fiber membrane as the separator. The electrolyte was 1.0 M $NaClO_4$ in EC and DMC (1:1, v/v) with 5 wt % fluoroethylene carbonate. The control cells of pPAN/S and pPAN/Se were prepared by the same method. The CV plots were recorded on an electrochemical workstation (CHI614b). Galvanostatic discharge-charge tests were measured on a Land battery measurement system (China). GITT was performed by discharging the cells for 10 min at $^1/_{30}$ C based on the stabilized capacity followed by a 5-min relaxation. For all electrochemical tests, the voltage range of Li-SeS_2 batteries is between 3.0 and 1.0 V versus Li/Li^+, while for RT Na-SeS_2 batteries the voltage range is 2.8 to 0.8 V versus Na/Na^+. The high loading Li-SeS_2 batteries were first cycled two times at 0.05 A g^{-1} for activation and then cycled at 0.2 A g^{-1}. The specific capacities and current densities of all cells were calculated based on the mass of SeS_2, S, or Se. The Nyquist plots were obtained at 5-mV ac oscillation amplitude from 100 kHz to 1 Hz.

SUPPLEMENTARY MATERIALS

Supplementary material for this article is available at http://advances.sciencemag.org/cgi/content/full/4/6/eaat1687/DC1

fig. S1. Schematic illustrations of the chemical structure and synthesis method.
fig. S2. EDX mappings of pPAN/SeS_2.
fig. S3. N_2 sorption isotherms of multichannel pPAN/SeS_2 fibers and pPAN/SeS_2 powder.
fig. S4. Morphology characterizations.
fig. S5. TGA curves of pPAN/S and pPAN/Se.
fig. S6. The active material contents of various PAN-supported or microporous carbon-supported composites for Li-S or Li-Se/S batteries.
fig. S7. EIS of pPAN/S, pPAN/SeS_2, and pPAN/Se.
fig. S8. Comparisons of capacity utilization and energy density for Li storage.
fig. S9. CV curves from 0.2 to 1.2 mV s^{-1}.
fig. S10. Rate performances.
fig. S11. Comparison of normalized capacities.
fig. S12. CV curves and voltage profiles of pPAN/SeS_2 for Na storage.
fig. S13. Comparisons of RT Na-S and Na-Se/S batteries.
References (*54*–*63*)

REFERENCES AND NOTES

1. B. Dunn, H. Kamath, J.-M. Tarascon, Electrical energy storage for the grid: A battery of choices. *Science* **334**, 928–935 (2011).
2. P. G. Bruce, S. A. Freunberger, L. J. Hardwick, J.-M. Tarascon, Li–O_2 and Li–S batteries with high energy storage. *Nat. Mater.* **11**, 19–29 (2012).
3. A. Manthiram, Y. Fu, S.-H. Chung, C. Zu, Y.-S. Su, Rechargeable lithium–sulfur batteries. *Chem. Rev.* **114**, 11751–11787 (2014).
4. Z. Li, H. B. Wu, X. W. Lou, Rational designs and engineering of hollow micro-/nanostructures as sulfur hosts for advanced lithium–sulfur batteries. *Energy Environ. Sci.* **9**, 3061–3070 (2016).

5. L. Ma, K. E. Hendrickson, S. Wei, L. A. Archer, Nanomaterials: Science and applications in the lithium–sulfur battery. *Nano Today* **10**, 315–338 (2015).
6. Z. Li, J. Zhang, B. Guan, D. Wang, L.-M. Liu, X. W. Lou, A sulfur host based on titanium monoxide@carbon hollow spheres for advanced lithium-sulfur batteries. *Nat. Commun.* **7**, 13065 (2016).
7. S. S. Zhang, Liquid electrolyte lithium/sulfur battery: Fundamental chemistry, problems, and solutions. *J. Power Sources* **231**, 153–162 (2013).
8. M. Barghamadi, A. S. Best, A. I. Bhatt, A. F. Hollenkamp, M. Musameh, R. J. Rees, T. Rüther, Lithium–sulfur batteries—The solution is in the electrolyte, but is the electrolyte a solution? *Energy Environ. Sci.* **7**, 3902–3920 (2014).
9. J. Wang, J. Yang, J. Xie, N. Xu, A novel conductive polymer-sulfur composite cathode material for rechargeable lithium batteries. *Adv. Mater.* **14**, 963–965 (2002).
10. J. Wang, L. Liu, Z. Ling, J. Yang, C. Wan, C. Jiang, Polymer lithium cells with sulfur composites as cathode materials. *Electrochim. Acta* **48**, 1861–1867 (2003).
11. B. Zhang, X. Qin, G. R. Li, X. P. Gao, Enhancement of long stability of sulfur cathode by encapsulating sulfur into micropores of carbon spheres. *Energy Environ. Sci.* **3**, 1531–1537 (2010).
12. S. Xin, L. Gu, N.-H. Zhao, Y.-X. Yin, L.-J. Zhou, Y.-G. Guo, L.-J. Wan, Smaller sulfur molecules promise better lithium–sulfur batteries. *J. Am. Chem. Soc.* **134**, 18510–18513 (2012).
13. Z. Li, L. X. Yuan, Z. Q. Yi, Y. M. Sun, Y. Liu, Y. Jiang, Y. Shen, Y. Xin, Z. L. Zhang, Y. H. Huang, Insight into the electrode mechanism in lithium-sulfur batteries with ordered microporous carbon confined sulfur as the cathode. *Adv. Energy Mater.* **4**, 1301473 (2014).
14. Y. Xu, Y. Wen, Y. J. Zhu, K. Gaskell, K. A. Cychosz, B. Eichhorn, K. Xu, C. Wang, Confined sulfur in microporous carbon renders superior cycling stability in Li/S batteries. *Adv. Funct. Mater.* **25**, 4312–4320 (2015).
15. S. Wei, L. Ma, K. E. Hendrickson, Z. Tu, L. A. Archer, Metal–sulfur battery cathodes based on PAN–sulfur composites. *J. Am. Chem. Soc.* **137**, 12143–12152 (2015).
16. H. B. Wu, S. Wei, L. Zhang, R. Xu, H. H. Hng, X. W. Lou, Embedding sulfur in MOF-derived microporous carbon polyhedrons for lithium–sulfur batteries. *Chem. Eur. J.* **19**, 10804–10808 (2013).
17. J. Hassoun, J. Kim, D.-J. Lee, H.-G. Jung, S.-M. Lee, Y.-K. Sun, B. Scrosati, A contribution to the progress of high energy batteries: A metal-free, lithium-ion, silicon–sulfur battery. *J. Power Sources* **202**, 308–313 (2012).
18. B. Duan, W. Wang, A. Wang, Z. Yu, H. Zhao, Y. Yang, A new lithium secondary battery system: The sulfur/lithium-ion battery. *J. Mater. Chem. A* **2**, 308–314 (2014).
19. S. S. Zhang, Sulfurized carbon: A class of cathode materials for high performance lithium/sulfur batteries. *Front. Energy Res.* **1**, 10 (2013).
20. J. Wang, Y.-S. He, J. Yang, Sulfur-based composite cathode materials for high-energy rechargeable lithium batteries. *Adv. Mater.* **27**, 569–575 (2015).
21. L. Wang, X. He, J. Li, J. Gao, J. Guo, C. Jiang, C. Wan, Analysis of the synthesis process of sulphur–poly(acrylonitrile)-based cathode materials for lithium batteries. *J. Mater. Chem.* **22**, 22077–22081 (2012).
22. L. Wang, X. He, J. Li, M. Chen, J. Gao, C. Jiang, Charge/discharge characteristics of sulfurized polyacrylonitrile composite with different sulfur content in carbonate based electrolyte for lithium batteries. *Electrochim. Acta* **72**, 114–119 (2012).
23. J. Fanous, M. Wegner, J. Grimminger, Ä. Andresen, M. R. Buchmeiser, Structure-related electrochemistry of sulfur-poly(acrylonitrile) composite cathode materials for rechargeable lithium batteries. *Chem. Mater.* **23**, 5024–5028 (2011).
24. J. Fanous, M. Wegner, J. Grimminger, M. Rolff, M. B. M. Spera, M. Tenzer, M. R. Buchmeiser, Correlation of the electrochemistry of poly(acrylonitrile)–sulfur composite cathodes with their molecular structure. *J. Mater. Chem.* **22**, 23240–23245 (2012).
25. L. Yin, J. Wang, F. Lin, J. Yang, Y. Nuli, Polyacrylonitrile/graphene composite as a precursor to a sulfur-based cathode material for high-rate rechargeable Li–S batteries. *Energy Environ. Sci.* **5**, 6966–6972 (2012).
26. L. Yin, J. Wang, J. Yang, Y. Nuli, A novel pyrolyzed polyacrylonitrile-sulfur@MWCNT composite cathode material for high-rate rechargeable lithium/sulfur batteries. *J. Mater. Chem.* **21**, 6807–6810 (2011).
27. H. Chen, C. Wang, C. Hu, J. Zhang, S. Gao, W. Lu, L. Chen, Vulcanization accelerator enabled sulfurized carbon materials for high capacity and high stability of lithium–sulfur batteries. *J. Mater. Chem. A* **3**, 1392–1395 (2015).
28. J. Ye, F. He, J. Nie, Y. Cao, H. Yang, X. Ai, Sulfur/carbon nanocomposite-filled polyacrylonitrile nanofibers as a long life and high capacity cathode for lithium–sulfur batteries. *J. Mater. Chem. A* **3**, 7406–7412 (2015).
29. Q. Li, H. Liu, Z. Yao, J. Cheng, T. Li, Y. Li, C. Wolverton, J. Wu, V. P. Dravid, Electrochemistry of selenium with sodium and lithium: Kinetics and reaction mechanism. *ACS Nano* **10**, 8788–8795 (2016).
30. G.-L. Xu, J. Liu, R. Amine, Z. Chen, K. Amine, Selenium and selenium–sulfur chemistry for rechargeable lithium batteries: Interplay of cathode structures, electrolytes, and interfaces. *ACS Energy Lett.* **2**, 605–614 (2017).
31. L. Zeng, W. Zeng, Y. Jiang, X. Wei, W. Li, C. Yang, Y. Zhu, Y. Yu, A flexible porous carbon nanofibers-selenium cathode with superior electrochemical performance for both Li-Se and Na-Se batteries. *Adv. Energy Mater.* **5**, 1401377 (2015).
32. H. Wang, S. Li, Z. Chen, H. K. Liu, Z. Guo, A novel type of one-dimensional organic selenium-containing fiber with superior performance for lithium–selenium and sodium–selenium batteries. *RSC Adv.* **4**, 61673–61678 (2014).
33. B. Yuan, X. Sun, L. Zeng, Y. Yu, Q. Wang, A freestanding and long-life sodium–selenium cathode by encapsulation of selenium into microporous multichannel carbon nanofibers. *Small* **14**, 1703252 (2018).
34. C.-P. Yang, S. Xin, Y.-X. Yin, H. Ye, J. Zhang, Y.-G. Guo, An advanced selenium–carbon cathode for rechargeable lithium-selenium batteries. *Angew. Chem. Int. Ed.* **52**, 8363–8367 (2013).
35. J. Ding, H. Zhou, H. Zhang, L. Tong, D. Mitlin, Selenium impregnated monolithic carbons as free-standing cathodes for high volumetric energy lithium and sodium metal batteries. *Adv. Energy Mater.* **8**, 1701918 (2018).
36. S. Xin, L. Yu, Y. You, H.-P. Cong, Y.-X. Yin, X.-L. Du, Y.-G. Guo, S.-H. Yu, Y. Cui, J. B. Goodenough, The electrochemistry with lithium versus sodium of selenium confined to slit micropores in carbon. *Nano Lett.* **16**, 4560–4568 (2016).
37. J. Ding, H. Zhou, H. Zhang, T. Stephenson, Z. Li, D. Karpuzov, D. Mitlin, Exceptional energy and new insight with a sodium–selenium battery based on a carbon nanosheet cathode and a pseudographite anode. *Energy Environ. Sci.* **10**, 153–165 (2017).
38. Y. Yao, L. Zeng, S. Hu, Y. Jiang, B. Yuan, Y. Yu, Binding $S_{0.6}Se_{0.4}$ in 1D carbon nanofiber with C—S bonding for high-performance flexible Li–S batteries and Na–S batteries. *Small* **13**, 1603513 (2017).
39. Y. Cui, A. Abouimrane, J. Lu, T. Bolin, Y. Ren, W. Weng, C. Sun, V. A. Maroni, S. M. Heald, K. Amine, (De)lithiation mechanism of Li/SeS_x (x = 0–7) batteries determined by in situ synchrotron X-ray diffraction and X-ray absorption spectroscopy. *J. Am. Chem. Soc.* **135**, 8047–8056 (2013).
40. I. Gomez, D. Mantione, O. Leonet, J. A. Blazquez, D. Mecerreyes, Hybrid sulfur–selenium co-polymers as cathodic materials for lithium batteries. *ChemElectroChem* **5**, 260–265 (2018).
41. J. Zhou, T. Qian, N. Xu, M. Wang, X. Ni, X. Liu, X. Shen, C. Yan, Selenium-doped cathodes for lithium–organosulfur batteries with greatly improved volumetric capacity and coulombic efficiency. *Adv. Mater.* **29**, 1701294 (2017).
42. Z. Li, J. T. Zhang, Y. M. Chen, J. Li, X. W. Lou, Pie-like electrode design for high-energy density lithium–sulfur batteries. *Nat. Commun.* **6**, 8850 (2015).
43. S. S. Zhang, Understanding of sulfurized polyacrylonitrile for superior performance lithium/sulfur battery. *Energies* **7**, 4588–4600 (2014).
44. J. Wang, J. Yang, C. Wan, K. Du, J. Xie, N. Xu, Sulfur composite cathode materials for rechargeable lithium batteries. *Adv. Funct. Mater.* **13**, 487–492 (2003).
45. J. Guo, Z. Wen, Q. Wang, J. Jin, G. Ma, A conductive selenized polyacrylonitrile cathode material for re-chargeable lithium batteries with long cycle life. *J. Mater. Chem. A* **3**, 19815–19821 (2015).
46. V. Augustyn, J. Come, M. A. Lowe, J. W. Kim, P.-L. Taberna, S. H. Tolbert, H. D. Abruña, P. Simon, B. Dunn, High-rate electrochemical energy storage through Li^+ intercalation pseudocapacitance. *Nat. Mater.* **12**, 518–522 (2013).
47. S. Xin, Y.-X. Yin, Y.-G. Guo, L.-J. Wan, A high-energy room-temperature sodium-sulfur battery. *Adv. Mater.* **26**, 1261–1265 (2014).
48. Z. Li, L. Yuan, Z. Yi, Y. Liu, Y. Huang, Confined selenium within porous carbon nanospheres as cathode for advanced Li–Se batteries. *Nano Energy* **9**, 229–236 (2014).
49. T. H. Hwang, D. S. Jung, J.-S. Kim, B. G. Kim, J. W. Choi, One-dimensional carbon–sulfur composite fibers for Na–S rechargeable batteries operating at room temperature. *Nano Lett.* **13**, 4532–4538 (2013).
50. S. Wei, S. Xu, A. Agrawral, S. Choudhury, Y. Lu, Z. Tu, L. Ma, L. A. Archer, A stable room-temperature sodium–sulfur battery. *Nat. Commun.* **7**, 11722 (2016).
51. D.-J. Lee, J.-W. Park, I. Hasa, Y.-K. Sun, B. Scrosati, J. Hassoun, Alternative materials for sodium ion–sulphur batteries. *J. Mater. Chem. A* **1**, 5256–5261 (2013).
52. A. Manthiram, X. Yu, Ambient temperature sodium–sulfur batteries. *Small* **11**, 2108–2114 (2015).
53. Z. Wen, Y. Hu, X. Wu, J. Han, Z. Gu, Main challenges for high performance NAS battery: Materials and interfaces. *Adv. Funct. Mater.* **23**, 1005–1018 (2013).
54. X. Li, J. Liang, K. Zhang, Z. Hou, W. Zhang, Y. Zhu, Y. Qian, Amorphous S-rich $S_{1-x}Se_x$/C ($x \leq 0.1$) composites promise better lithium–sulfur batteries in a carbonate-based electrolyte. *Energy Environ. Sci.* **8**, 3181–3186 (2015).
55. L. Zeng, Y. Yao, J. Shi, Y. Jiang, W. Li, L. Gu, Y. Yu, A flexible $S_{1-x}Se_x$@porous carbon nanofibers ($x \leq 0.1$) thin film with high performance for Li-S batteries and room-temperature Na-S batteries. *Energy Storage Mater.* **5**, 50–57 (2016).
56. J. L. Wang, J. Yang, J. Y. Xie, N. X. Xu, Y. Li, Sulfur–carbon nano-composite as cathode for rechargeable lithium battery based on gel electrolyte. *Electrochem. Commun.* **4**, 499–502 (2002).
57. X.-G. Sun, X. Wang, R. T. Mayes, S. Dai, Lithium-sulfur batteries based on nitrogen-doped carbon and an ionic-liquid electrolyte. *ChemSusChem* **5**, 2079–2085 (2012).
58. Z. Zhang, Z. Li, F. Hao, X. Wang, Q. Li, Y. Qi, R. Fan, L. Yin, 3D interconnected porous carbon aerogels as sulfur immobilizers for sulfur impregnation for lithium-sulfur batteries with high rate capability and cycling stability. *Adv. Funct. Mater.* **24**, 2500–2509 (2014).
59. Y.-X. Wang, J. Yang, W. Lai, S.-L. Chou, Q.-F. Gu, H. K. Liu, D. Zhao, S. X. Dou, Achieving high-performance room-temperature sodium–sulfur batteries with S@interconnected mesoporous carbon hollow nanospheres. *J. Am. Chem. Soc.* **138**, 16576–16579 (2016).

60. C. Luo, Y. Zhu, O. Borodin, T. Gao, X. Fan, Y. Xu, K. Xu, C. Wang, Activation of oxygen-stabilized sulfur for Li and Na batteries. *Adv. Funct. Mater.* **26**, 745–752 (2016).
61. Q. Lu, X. Wang, J. Cao, C. Chen, K. Chen, Z. Zhao, Z. Niu, J. Chen, Freestanding carbon fiber cloth/sulfur composites for flexible room-temperature sodium-sulfur batteries. *Energy Storage Mater.* **8**, 77–84 (2017).
62. S. Zheng, P. Han, Z. Han, P. Li, H. Zhang, J. Yang, Nano-copper-assisted immobilization of sulfur in high-surface-area mesoporous carbon cathodes for room temperature Na-S batteries. *Adv. Energy Mater.* **4**, 1400226 (2014).
63. R. Carter, L. Oakes, A. Douglas, N. Muralidharan, A. P. Cohn, C. L. Pint, A sugar-derived room-temperature sodium sulfur battery with long term cycling stability. *Nano Lett.* **17**, 1863–1869 (2017).

Acknowledgments
Funding: X.W.L. is grateful to the Office of Naval Research Global (US) for financial support through the Naval Research Grant (N62909-17-1-2162, M4062262). **Author contributions:** Z.L. and X.W.L. conceived the idea and co-wrote the manuscript. Z.L. and J.Z. carried out the materials synthesis and the electrochemical evaluation. J.Z. and Y.L. helped with materials characterizations. All the authors discussed the results and commented on the manuscript. **Competing interests:** The authors declare that they have no competing interests. **Data and materials availability:** All data needed to evaluate the conclusions in the paper are present in the paper and/or the Supplementary Materials. Additional data related to this paper may be requested from the authors.

Submitted 31 January 2018
Accepted 26 April 2018
Published 8 June 2018
10.1126/sciadv.aat1687

Citation: Z. Li, J. Zhang, Y. Lu, X. W. Lou, A pyrolyzed polyacrylonitrile/selenium disulfide composite cathode with remarkable lithium and sodium storage performances. *Sci. Adv.* **4**, eaat1687 (2018).